RESEARCH ARTICLE

physica status solidi b
www.pss-b.com

Molybdenum Induced Modifications in the Quantum Capacitance of Graphene-Based Supercapacitor Electrodes: First-Principle Calculations

*David Ansi, Henry Martin, Linus K. Labik, Abu Yaya, Van W. Elloh, and Eric K. K. Abavare**

Herein, spin-polarized calculation is performed based on density-functional theory in the frame of generalized gradient approximation to examine the quantum capacitance (C_Q) and surface charge storage of graphene(G)-based supercapacitor electrodes modified with molybdenum, sulfur, nitrogen, and monovacancy. In total, 15 electrode models, including graphitic doping, monovacancy doping, and Mo adsorption on pristine and single-vacancy graphene structures are analyzed. In the results, it is demonstrated that vacancy defects and N/S/Mo doping enhances the C_Q of graphene. Among all configurations, pyrrolic-S (d1S) shows the lowest C_Q performance due to few states at the Fermi level. Electrodes with Mo adsorption exhibit the highest C_Q, particularly when Mo is adsorbed at the top site of graphene. However, formation and adsorption energy calculations suggest that Mo is more likely to adsorb at hollow sites. Optimally, Mo can be most effectively utilized by loading it onto vacancy or N/S-decorated vacancy sites. The significant contribution of Mo's $4dz^2$ and 4s states to C_Q, along with the charge-redistribution around the Mo complexes, may facilitate proton-coupled electron transfer to enhance pseudocapacitance. In these findings, valuable insights into designing high quantum capacitance of 2D materials with electroactive sites for improved energy storage are offered.

1. Introduction

Electrochemical double-layer capacitors (EDLCs) are a type of supercapacitor (mostly carbon based) with superior power density and long cycle life due to fast physical surface processes. However, they have low energy density when compared to batteries.[1] In most applications, the capacity of EDLCs is generally too small and its performance is hindered partly because of reduced effective surface area and/or limited electrolyte access to the electrode materials.[2–5] When using aqueous electrolytes, these capacitors only store a small fraction of electrons (around 0.17–0.2 atom^{-1}. Compared with 1–3 localized electrons per atom in battery materials).[6] Since electrode materials are active materials in supercapacitors, screening suitable materials for supercapacitor applications is crucial for achieving enhanced capacity.

Graphene has been significantly studied both experimentally and theoretically ever since its discovery in 2004 due to the uniqueness of its electronic, chemical, and physical properties.[7–9] By isolating a single layer of graphite, graphene, a 2D honeycomb lattice of carbon atoms, can be synthesized. The material has wide technological utility with potential application in electrochemical storage devices, where it can be used as anode material of rechargeable lithium batteries or as supercapacitor electrodes.[10–13] Theoretically, the high surface area (2630 m^2 g^{-1}) of graphene should attain a gravimetric capacitance of ≈550 Fg^{-1}, making it an ideal active material for EDLCs.[14]

In practical implementation of low-dimensional carbon-based materials like nanostructured activated carbon and graphene, studies report that the total capacitance (C_T) of such supercapacitors involves contributions arising from the electrode/electrolyte interface (C_{EE})—which could be double-layer capacitance and/or pseudocapacitance—and an inherent capacitance of the electrode (quantum capacitance C_Q).[15–17] Performance of graphene supercapacitors at small potentials, for instance, is reported to be limited by the material's low C_Q.[18,19] However, enhancement of capacitance observed for nitrogen-doped graphene electrodes was attributed to the improvement of quantum capacitance (C_Q) and the introduction of pseudocapacitive active sites (this is particularly true when aqueous electrolytes are used because pseudocapacitance is present as a result of the reversible protonation of these active sites).[20,21]

D. Ansi, H. Martin, L. K. Labik, E. K. K. Abavare
Department of Physics
Kwame Nkrumah University of Science and Technology
Kumasi, Ghana
E-mail: ekkabavare.cos@knust.edu.gh

A. Yaya
Department of Materials Science and Engineering
University of Ghana
Accra, Ghana

V. W. Elloh
Department of Biomedical Engineering
Koforidua Technical University
Koforidua, Ghana

The ORCID identification number(s) for the author(s) of this article can be found under https://doi.org/10.1002/pssb.202400459.

DOI: 10.1002/pssb.202400459

The C_Q of a material is related to its density of states (DOS). Experiments have been undertaken to map the electronic DOS of 2D materials directly through quantum capacitance measurement.[22] It is therefore possible for the intrinsic capacitance (C_Q) of a material to be modified by defects, strains, functional groups, dopant atoms, or adsorbates—either intentionally by chemical treatment or through the process of synthesis. Many reports have shown that doping or functionalizing graphene is an effective way to enhance its performance in supercapacitors.[23–25]

First-principle calculations in the framework of density functional theory (DFT) are carried out in this study to investigate the impact of molybdenum-induced modifications on the electronic structure and quantum capacitance of graphene electrodes, drawing inspiration from structural motifs observed in molybdenum cofactor in nitrogenase.[26,27] The complexes observed in nitrogenase enzymes, studied for electrocatalytic nitrogen reduction (NRR),[26,27] include molybdenum atoms surrounded by sulfur (S) or nitrogen (N) atoms. Thus, a range of modifications are systematically explored in this article involving molybdenum (Mo), sulfur (S), nitrogen (N), and single vacancy. This systematic approach has experimental significance: after synthesis, the Mo, N, or S codoped graphene is likely to have a complex structure with various defects and dopant configurations present as shown in ref. [28]. These defects and configurations may include vacancy defects, Mo atoms adsorbed on various sites of the graphene surface, and substitution of carbon atoms by dopant atoms (including configurations like graphitic N/S and pyridinic N/S). The study aims to enhance the performance of supercapacitors through the design of high C_Q graphene electrode materials with active sites for surface redox processes. On the basis of formation energy calculation, the stability of the electrode models is also discussed. The work is summarized as follows: 1) Introduction, 2) Computational methodologies, 3) Results and discussion, and 4) Conclusion.

2. Computational Methodology

The surface charge, Q, of the uncharged graphene electrode is given by the following equation

$$Q = e\int_{-\infty}^{+\infty} \mathrm{DOS}(E) f(E)\,\mathrm{d}E \tag{1}$$

Assuming that the electronic structure (DOS) of the electrode is not altered by the charging process (ϕ)—that is, the fixed-band approximation[29]—the excess surface charge density, Q_{SCD} after applying potential, ϕ becomes

$$Q_{SCD} = e\int_{-\infty}^{+\infty} \mathrm{DOS}(E)[f(E) - f(E+e\phi)]\,\mathrm{d}E \tag{2}$$

where e is the elementary charge, E is the energy, ϕ is the applied voltage on the electrode, and $f(E)$ is the Fermi–Dirac distribution function. Quantum capacitance (C_Q) is obtained as the variation of the excess surface charge density (Q_{SCD}) with respect to the applied potential (ϕ)

$$C_Q = \frac{dQ_{SCD}}{d\phi} = \frac{e^2}{4kT}\int_{-\infty}^{+\infty} \mathrm{DOS}(E)\mathrm{sech}^2\left[\frac{E+e\phi}{2kT}\right]\mathrm{d}E \tag{3}$$

Using an electronic structure method to obtain DOS, C_Q can be obtained. Several studies have successfully employed Hohenberg and Kohn formulation[30,31] for the computation of C_Q of graphene. While more realistic outcomes can be obtained with a framework that includes electronic structure changes, it will suffice for this research because it is shown to be valid for monolayer graphene and also useful, as a first approximation, in providing quick estimations.[32] We performed spin polarized DFT calculations within the generalized gradient approximation using Perdew–Burke–Ernzerhof (GGA–PBE) functional as implemented in Quantum ESPRESSO[33] to describe the many-body electron–electron effects. The nuclear and core interactions were described using ultrasoft pseudopotential schema based on Kresse–Joubert projector-augmented wave (PAW)[34,35] method, which considerably reduces the number of plane waves. The wavefunction of valence electron density was expanded in plan waves and Kohn–Sham orbitals solved using the Davidson iterative diagonalization procedure in the framework of pseudopotential approximation. The charge density update was performed using the modified Broyden description[36] and determined the kinetic energy cutoff to 100 Ry following a test to assure the accuracy of calculations. The Brillouin zone was sampled at mesh k-point mesh of $16 \times 16 \times 1$ using the Monkhorst Pack grid of the supercell. Structural optimization was carried out on all the structures using the Broyden–Fletcher–Goldfarb–Shanno (BFGS) algorithm[37] until all atoms were fully relaxed with Hellman–Feynman forces less than 10^{-3} (a.u) on each atom. The Marzari–Vanderbilt smearing approach[38] was used with a smearing energy of 0.01 Ry for all calculations. The kinetic energy cutoff for all calculations did not exceed 100 Ry and vacuum slab thickness of about 30 Å. A $3 \times 3 \times 1$ supercell with a lattice constant of 7.386 Å after testing was used for all structural models.

3. Results and Discussion

3.1. Pristine Graphene with One Atom Substituted with Mo, S, and N

The optimized structures for pristine, N-, S-, and Mo-doped graphene are shown in **Figure 1**a–d, with the corresponding calculated parameters in **Table 1**. The quantum capacitance (C_Q) and excess surface charge density (Q_{SCD}) of pristine graphene, as well as N-doped (NG), S-doped (SG), and Mo-doped (MoG) graphene, are depicted in **Figure 2**A(a–c). In line with the fixed band approximation, the C_Q behavior directly follows from the DOS at the Fermi level. Consequently, pristine graphene shows a symmetric U-shaped C_Q profile, with a minimum value of 1.04 μF cm^{-2} at 0.00 V, close to the theoretical result of 1.10 μF cm^{-2} reported by Yang et al.[20] In contrast, the C_Q of all doped systems fluctuates and exhibits asymmetric behavior. The N-doped graphene system has a camel-like shape, peaking at −0.16 V with a maximum C_Q of 77.64 μF cm^{-2}. The S-doped graphene reaches its maximum C_Q at 0.06 V, with a value of 87.14 μF cm^{-2}. For both SG and NG, the Q_{SCD} under positive charging is lower than that

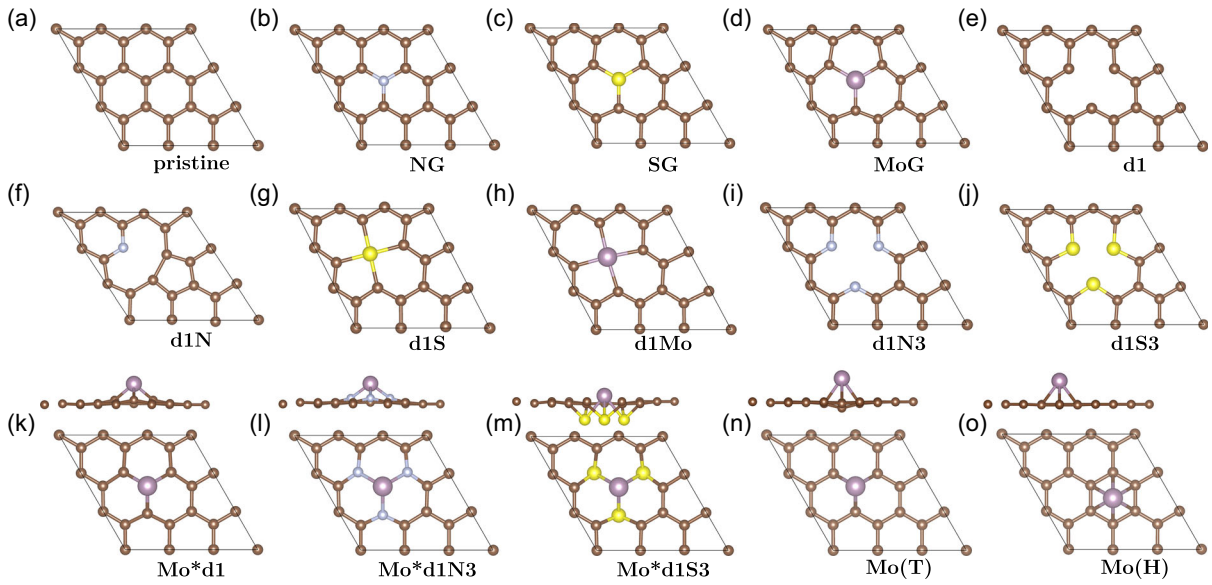

Figure 1. Geometric structure of pristine and modified graphene. a) Reference 3 × 3 graphene supercell. b) N-doped, NG; c) S-doped, SG; and d) Mo-doped graphene, MoG. e) Single vacancy, d1; f) single N atom at vacancy site, d1N; g) single S at vacancy site, d1S; h) single Mo at vacancy site, d1Mo. i,j) Three N/S atoms substituting the unsaturated carbon atoms d1N3/d1S3. k) Mo anchored on single vacancy, Mo*d1. l,m) Mo anchored on N/S decorated monovacancy, Mo*d1N3/Mo*d1S3. n) Mo adsorbed on top site of graphene, Mo(T). o) adsorbed on hollow site of graphene, Mo(H). Brown, carbon (C); blue, nitrogen (N); yellow, sulfur (S); purple, molybdenum (Mo).

Table 1. Bond lengths (d_1, d_2, and d_3), height of Mo above the graphene plane (h), the maximum quantum capacitance (C_{Qmax}), total magnetic moment of systems (M_{tot}), and Löwdin charge (Q_L) of dopant atom.

Systems	d_1 [Å]	d_2 [Å]	d_3 [Å]	h [Å]	C_{Qmax} [μF cm^{-2}]	M_{tot} [μ_B]	Q_L [∈]	Space group
Pristine	1.424	1.424	1.424	–	17.33	0.00	–	D_{6h}
NG	1.413	1.413	1.413	–	77.64	0.00	0.0099	D_{3h}
SG	1.661	1.661	1.661	–	87.14	0.08	−0.9779	D_{3h}
MoG	1.804	1.804	1.804	–	126.81	1.96	−0.7674	C_{3v}
d1	–	–	–	–	83.19	1.05	–	C_{2v}
d1N	1.313	1.313	–	–	98.60	0.00	0.2250	C_s
d1S[a)]	1.880	1.880	–	–	23.31	0.00	−0.7792	C_s
d1Mo[a)]	1.992	2.067	–	–	110.07	2.37	−1.0847	C_s
d1N3	1.343	1.343	–	–	98.84	0.80	0.1646	D_{3h}
d1S3	1.698	1.698	–	–	70.93	0.00	−0.4732	D_{3h}
Mo*d1	1.926	1.926	–	1.4519	136.98	2.00	−0.6539	C_{3v}
Mo*d1N3	1.907	1.907	1.907	1.4479	127.12	1.06	−0.7084	C_{3v}
Mo*d1S3	2.351	2.351	2.351	0.4136	174.64	0.00	−0.5513	C_{3v}
Mo(T)	2.251	2.251	2.251	2.059	122.62	3.98	−0.5469	C_{3v}
Mo(H)	2.203	2.202	2.202	1.665	206.16	0.00	−0.4783	C_{6v}

[a)]There are four bonds which exhibit symmetry. As a result, the bond lengths can be grouped into two pairs, with each pair having identical bond lengths.

under negative charging, indicating a greater accumulation of excess charge at the negative electrode.

N and S dopants introduce states at the Fermi level, leading to an increase in C_Q due to the higher density of electronic states. The DOS of NG and SG resembles that of pristine graphene, with the Fermi level moved up by ≈1.00 eV (**Figure 3**). The additional valence electrons from N and S atoms contribute to a higher electron density, shifting the Fermi level upward as electrons are donated to the π^* band. This increased electron density at the Fermi level enhances C_Q. The lower surface charge on SG and NG cathode is attributed to the low density and delocalized nature of π electrons below the Fermi level. The symmetry of the

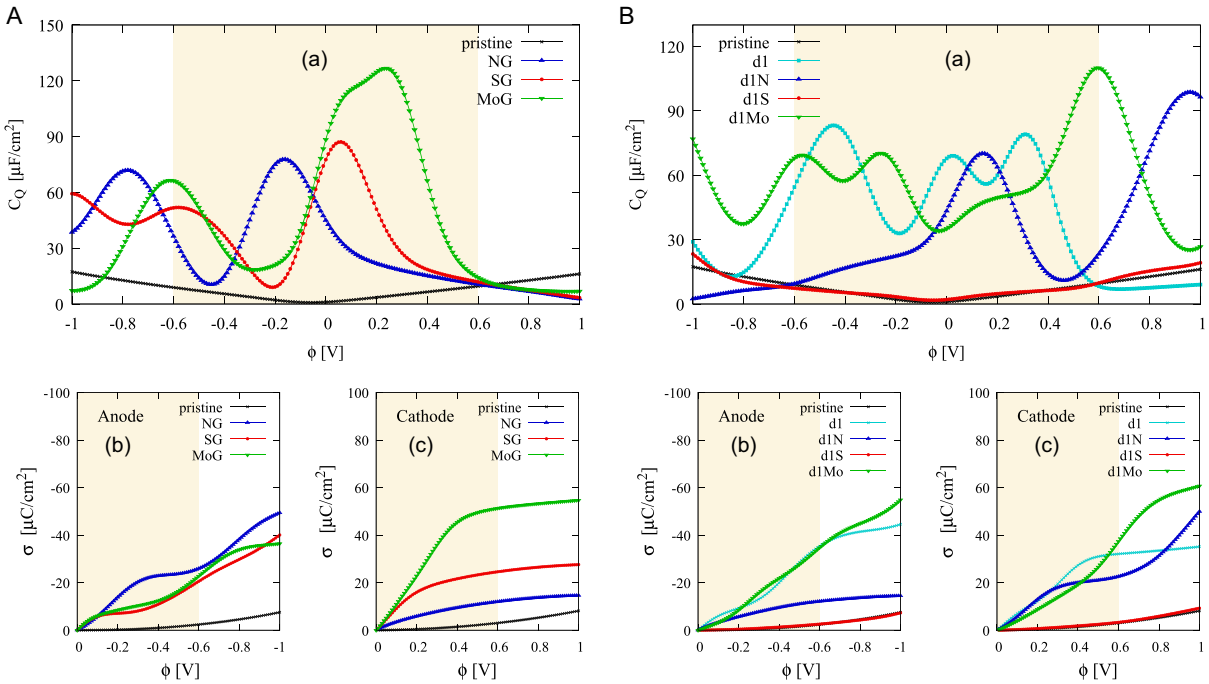

Figure 2. a) Quantum capacitance and b,c) excess surface charge density plots of pristine A) NG, SG, and MoG and B) d1, d1N, d1S, and d1Mo. The yellow region is the voltage range within which aqueous systems remain stable.

up and down spin DOS indicates that NG is nonmagnetic; however, Table 1 reveals a small magnetic moment of 0.08 μ_B for the SG electrode.

Molybdenum doping (MoG) has the highest C_Q at 0.24 V (126.81 μF cm^{-2}), resulting in increased charge accumulation on the positive electrode (Figure 2A(c)). The enhancement is linked to new states introduced in the valence band near the Fermi level, resulting from the hybridization between the Mo atom and the *p*-states of graphene. The up-spin and down-spin DOS are asymmetrical, indicating the material is magnetic, with a magnetic moment of 1.96 μ_B. Mo doping enhances graphene's quantum capacitance more effectively than N or S doping.

The C_Q and Q_{SCD} of these doped systems show significant enhancements, particularly at voltages below 0.60 V. This voltage range coincides with the potential window of aqueous electrolytes (−0.6 to 0.6 V) and is crucial for the performance of supercapacitors. In this region, the increased capacitance means that the overall capacitance of the graphene supercapacitor will no longer be dominated by the low C_Q of pristine graphene. This change translates to improved energy and power densities, which are essential for efficient energy storage applications. Overall, the asymmetrical quantum capacitance profiles of N-, S-, and Mo-doped graphene make them promising active cathode or anode materials for asymmetric supercapacitors, due to their higher C_Q compared to pristine graphene at positive or negative voltages.

3.2. Single Vacancy-Defect Graphene with N, S, and Mo Doping

The most common defect occurring during the synthesis of graphene is a vacancy. Atoms can be substitutionally doped at carbon sites of the vacancy region. Therefore, the C_Q of the dopant atoms within vacancy-defect graphene is investigated here. The single vacancy-defect graphene, labeled as d1, is depicted in Figure 1e. Substitutional doping with nitrogen (N), sulfur (S), and molybdenum (Mo) into vacancy-defect graphene results in structures denoted as d1N, d1S, and d1Mo, respectively, which are shown in Figure 1f–h. Table 1 shows the calculated parameters. Five member rings are observed in Figure 1f–h: d1N is a pyridinc-N structure with a carbon pentagon ring formed due to bonding between the two carbon atoms of the vacancy. d1S and d1Mo are pyrrolic-S/Mo and have no unbonded atoms.

Unlike pristine graphene, which exhibits a symmetric U shape C_Q, single vacancy (d1) shows an asymmetric and well-enhanced C_Q, reaching 67.83 μF cm^{-2} at 0.00 V. The highest C_Q (83.18 μF cm^{-2}) occurs at −0.45 V. Although the quantum capacitance is lower above 0.60 V compared to ideal graphene electrodes, the surface charge is significantly higher than in pristine graphene. The increased C_Q within ±0.6 V suggests that vacancy defects can enhance charge storage performance in graphene electrodes by improving the inherent capacitance contribution to total capacitance. The differing C_Q behavior between the positive and negative voltage regions also makes it a promising candidate for asymmetric supercapacitor electrodes.

From the DOS shown in Figure 3e, the capacitance enhancement in d1 arises from semilocalized states associated with the unbonded carbon atoms. These states originate from interactions between the sp^2 and p_z orbitals of the three carbon atoms surrounding the vacancy, consistent with findings in ref. [20]. The d1 structure has a magnetic moment of 1.05 μ_B.

Upon introducing the N/S dopant (d1N/d1S systems), C_Q and the electrode excess surface charge density for both N and S

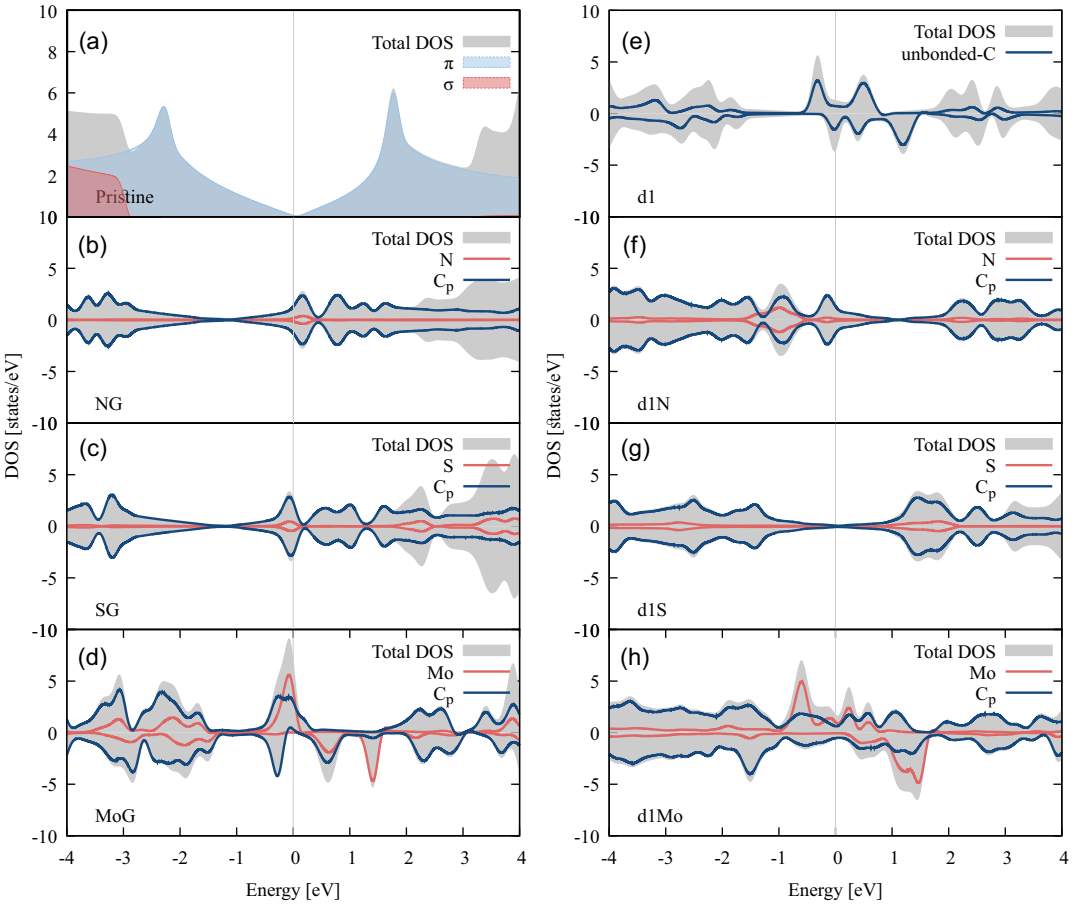

Figure 3. Density of states (DOS) of a) pristine, b) NG, c) SG, d) MoG, e) d1, f) d1N, g) d1S, and h) d1Mo.

systems are lower at the anode compared to the vacancy defect electrode. Nitrogen doping results in reduced performance at higher negative voltages (beyond −0.60 V) but significantly improves capacitance at the positive electrode, peaking at 98.56 μF cm^{-2} at 0.96 V. The d1N electrode will be a better candidate as cathode material for asymmetric supercapacitors. DOS of d1N, shown in Figure 3, resembles pristine graphene, with the E_f shifted (by 0.97 eV) into the valence band because of electron deficiency. Unpaired sp^2 orbital of pyridin-N contributes states in the valence band. The two adjacent C atoms of the vacancy bond together and only contribute their p_z electrons to states few eV below the E_f. These states account for the better C_Q performance at the cathode.

S-doped vacancy defect exhibits a symmetric U-shaped C_Q, similar to pristine graphene (Figure 2B(a)), with a C_Q value of 2.06 μF cm^{-2} (0.00 V), compared to 1.04 μF cm^{-2} (0.00 V) for pristine. The reason, unlike d1 and d1N, may be attributed to the absence of localized states associated with the unbonded C atoms near the E_f, as reflected in the optimized structure. The LDOS shows S contributes states that are far away from the Fermi level, suggesting that the realigned sp^2 and p_z orbitals mainly form in-plane bonds which partake in the structural property rather than the electronic property of the material. C_Q of d1S is small and would limit the total capacitance.

For d1Mo, the maximum C_Q is 110.07 μF cm^{-2} at 0.60 V. It also exhibits high excess surface charge density at both anode and cathode, with the values of −54.90 μC cm^{-2} and 60.76 μC cm^{-2}. LDOS (Figure 3h) reveals that the high C_Q is mainly due to localized states from the molybdenum atom and *p*-orbitals of carbon. This finding suggests that d1Mo can serve as a promising cathode or anode material for asymmetric supercapacitors. d1Mo is spin polarized with a magnetic moment of 2.37 μ_B.

3.3. Single Vacancy (d1) with Mo Adsorbed over the Vacancy Site, Single Vacancy with N3 and S3

Next, we examine the substitution of three nitrogen/sulfur (d1N3/d1S3) atoms at the vacancy site and explore molybdenum adsorption on single vacancy graphene (Mo*d1). Optimized structures are shown in Figure 1i–k.

From **Figure 4**C, maximum capacitance values are 98.84 μF cm^{-2} (0.41 V) for d1N3, 70.92 μF cm^{-2} (−0.28 V) for d1S3, and 136.98 μF cm^{-2} (−0.76 V) for Mo*d1. Although d1N3 accumulates the most excess charge at the positive electrode, Mo*d1 exhibits the highest C_Q in general. The d1N3 anode capacitance is very low above −0.20 V because of the low-density delocalized π states of the conduction band. Similar to d1, the sp^2

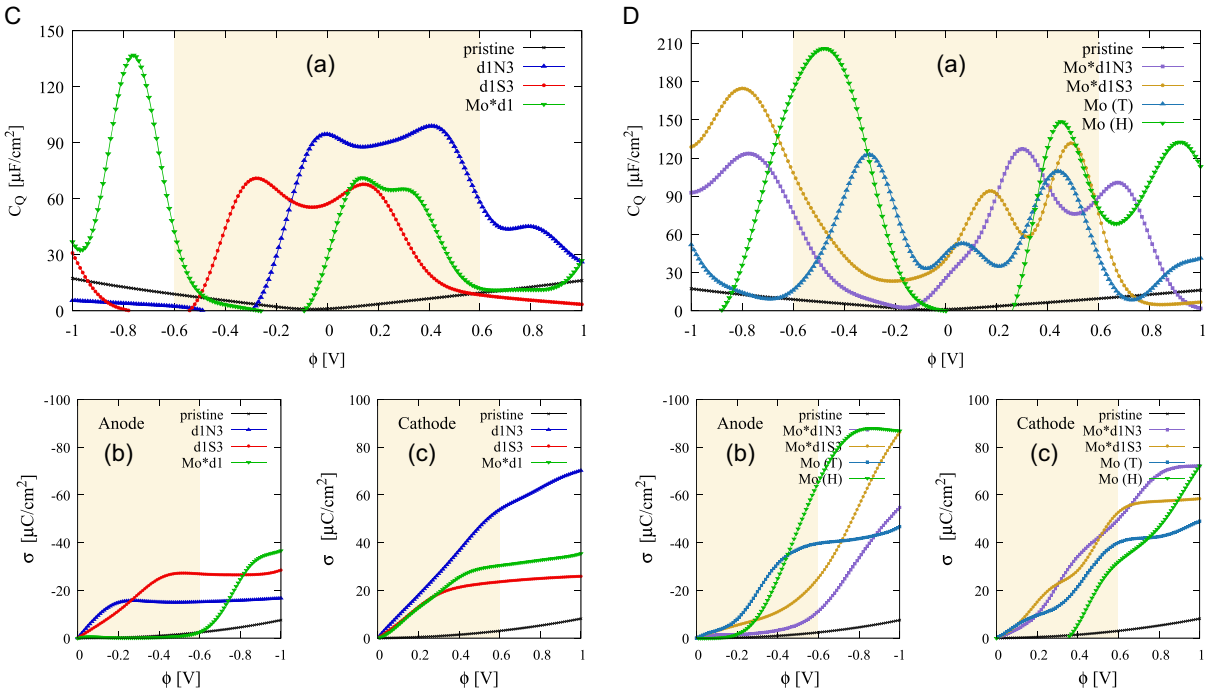

Figure 4. a) Quantum capacitance and b,c) excess surface charge density plots of pristine C) d1N3, d1S3, and Mo*d1 and D) Mo*d1N3, Mo*d1S3, Mo(T), and Mo(H). The yellow region is the voltage range within which aqueous systems remain stable.

and p_z of the three adjacent nitrogen atoms couple to form localized defect states at the Fermi level. These local states cause spin polarization and also lead to the enhancement of C_Q at the positive electrode.

The similar C_Q behavior between the positive and negative voltage regions in d1S3 resulted in an almost symmetric C_Q enhancement within a window of ≈0.9 V (−0.45 to 0.45 V), suggesting its potential for symmetric electrodes. But capacitance drops outside this range, with zero capacitance between −0.8 and −0.6 V (regions of zero capacitance are also present at the anode for d1N3 and Mo*d1)—this is a result of band gap in the conduction band. The DOS (**Figure 5**) resembles pristine graphene with the Fermi level shifted 0.83 eV into the conduction band because extra electrons are injected into the π^* band (74 electrons per unit cell in d1S3 versus 72 electrons/unit cell in pristine). The capacitance enhancement is due to the p_z orbitals of the S atoms. Unlike d1 and d1N3, the sp^2 orbitals did not form localized states in the energy range of interest and the structure is nonmagnetic.

Mo adsorption (Mo*d1) showed the highest quantum capacitance value in this group. But it exhibits poor capacitance between −0.50 and −0.10 V, corresponding to regions of low density of states. In the working voltage of aqueous electrolytes, this material would be undesirable as an anode material—considering no excess surface charge accumulated between 0.00 and −0.60 V—but can serve as a cathode material. The high C_Q is due to strongly localized d-states from Mo. Both d1N3 and Mo*d1 hold potential as cathode materials for asymmetric supercapacitors, while d1S3's symmetric behavior suggests its applicability as an active electrode material for symmetric supercapacitors.

3.4. Mo Loaded on Single Vacancy Decorated with Three N Atoms (d1N3) and Three S Atoms (d1S3)

d1S3 and d1N3 doping structures are considered to support the single Mo atom (Mo*d1N3 and Mo*d1S3), resembling nitrogenase-like structures.[26] The optimized geometries are shown in Figure 1l,m. Both Mo*d1S3 and Mo*d1N3 electrodes exhibit similar trends in capacitance performance. At negative voltages, C_Q dips between about 0.20 and −0.60 V, forming a U-shaped curve. The maximum capacitance at the anode occurs at −0.77 V (123.42 μF cm^{-2}) for Mo*d1N3 and at −0.80 V (174.63 μF cm^{-2}) for Mo*d1S3. At the cathode, the peak capacitance is 131.64 μF cm^{-2} (0.49 V) for Mo*d1S3 and 0.30 V (127.12 μF cm^{-2}) for Mo*d1N3. The surface charge behavior mirrors the capacitance results, with few charges accumulating at small voltages at the anode, followed by a steady increase above −0.60 V, and linear accumulation at the cathode. This suggests that both Mo*d1S3 and Mo*d1N3 could serve as cathode materials for supercapacitors (SCs) and as potential anode materials under higher-voltage conditions.

The enhancement in C_Q is linked to the density of states (DOS) profiles shown in Figure 5. The localized states found 1.00 eV below the Fermi level contribute to improved capacitance at the cathode, while the limited capacitance at low anode voltages is due to insufficient states few eV into the conduction band. A higher number of states near 1.00 eV results in better capacitance at higher voltages. In both Mo*d1N3 and Mo*d1S3, molybdenum contributes the most to the states within the energy range of interest (±1.00 eV), with carbon contributing slightly less, and nitrogen or sulfur contributing even less.

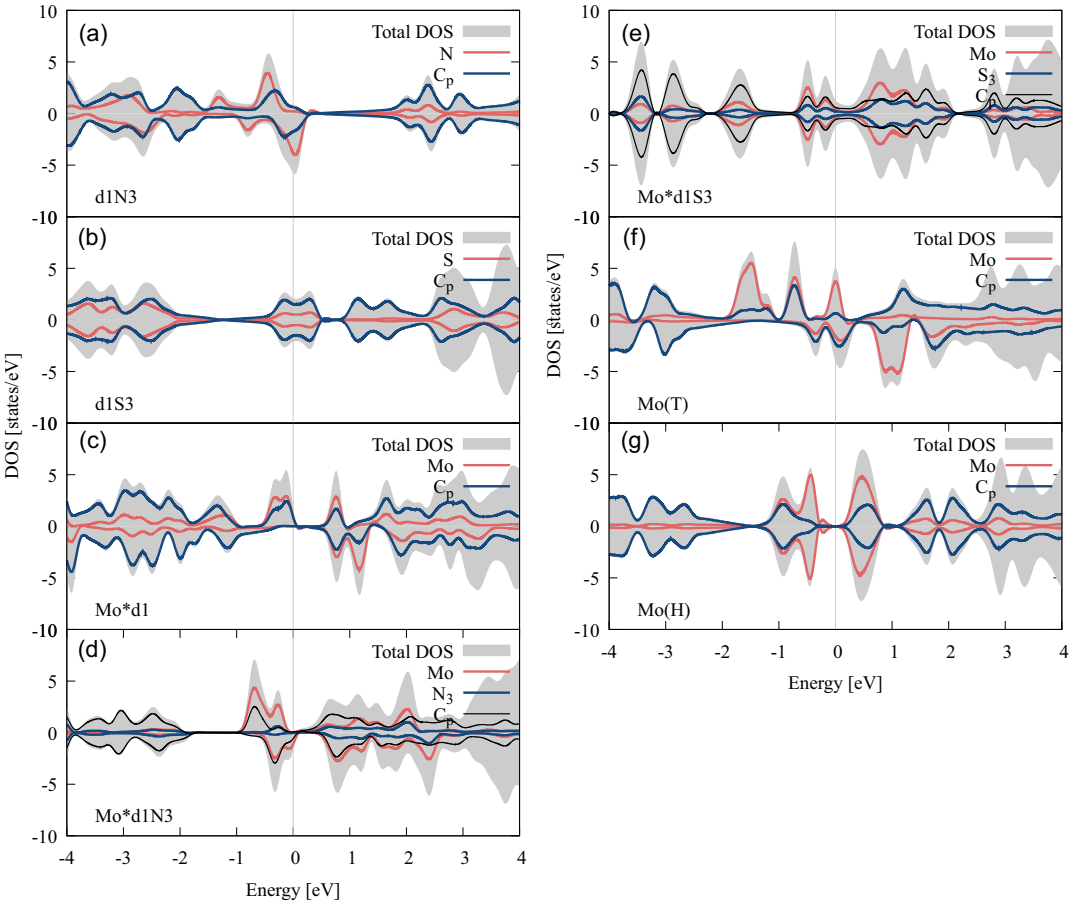

Figure 5. Density of states of a) d1N3, b) d1S3, c) Mo*d1, d) Mo*d1N3, e) Mo*d1S3, f) Mo(T), and g) Mo(H).

While Mo*d1N3 exhibits magnetism with a magnetic moment of 1.06 μ_B, Mo*d1S3 is nonmagnetic, likely due to the presence of sulfur atoms, as sulfur atoms tend to quench magnetic moments.[39]

3.5. Pristine Graphene with Mo Adsorbed on Top Site and Hollow Site

The optimized structures of this group are shown in Figure 1n,o. Table 1 shows the calculated parameters. The voltage variation of C_Q for each configuration is shown in Figure 4. The Mo(T) configuration exhibits a "Batman"-shaped capacitance curve,[40] with a bump at 0.00 V (52.68 μF cm^{-2}) and peak values of 109.41 μF cm^{-2} (0.44 V) and 122.62 μF cm^{-2} (−0.30 V). The almost symmetric surface charge behavior suggests that Mo(T) could be a suitable electrode material for symmetric SCs.

The Mo(H) configuration generally exhibits higher capacitance than Mo(T). At negative voltages, the C_Q curve is bell shaped, with a maximum value of 206.16 μF cm^{-2} (−0.48 V). On the positive side, maximum values of 132.66 μF cm^{-2} at 0.92 V and 148.64 μF cm^{-2} at 0.45 V are observed. The anode surface charge for Mo(H) outperforms the Mo(T) structure from around −0.40 V. Mo(H) behaves asymmetrically and performs well as an anode for asymmetric SCs at negative voltages and as a cathode at positive voltages. However, it performs poorly at low voltage conditions because of the presence of a bandgap, which results in zero excess charge near 0.00 V.

The DOS in Figure 5 reveals that the high capacitance for Mo(T) and Mo(H) is largely due to states from the molybdenum atoms and partially from the *p*-orbitals of carbon. Mo(T) is nonmagnetic, while Mo(H) is magnetic, with a magnetic moment of 3.98 μ_B.

Overall, molybdenum and carbon atoms exert the greatest influence near the Fermi level, enhancing the quantum capacitance performance. A summary of the C_Q results for all 15 models is presented in Table 1, which shows that molybdenum-based systems exhibit the highest C_Q values, with Mo positioned at a top site yielding the best C_Q.

3.6. Charge Density Difference and Band Structure Analysis

Given that electrode models with molybdenum exhibit the highest quantum capacitance (C_Q) values, we focus on these models to investigate the Mo-induced modifications further. To understand the mechanism behind the quantum capacitance enhancement caused by molybdenum, we examine the charge density difference (CDD) and *k*-resolved band structure.

3.6.1. Charge Density Difference Analysis

The results of the Löwdin charges (Q_L) presented in Table 1 are negative for molybdenum, indicating that the Mo atom primarily acts as an electron donor to the surrounding system. This behavior is consistent with the CDD plots shown in **Figure 6**, where charge depletion is observed on the molybdenum atom and corresponding charge accumulation occurs on the neighboring atoms. The density difference is given as

$$\Delta\rho(\mathbf{r}) = \rho(\mathbf{r}) - \rho_{\text{gra-sub}}(\mathbf{r}) - \rho_{\text{Mo}}(\mathbf{r}) \quad (4)$$

where $\rho(\mathbf{r})$ is the electron density of the Mo/graphene system and $\rho_{\text{gra}-\text{sub}}(\mathbf{r})$ and $\rho_{\text{Mo}}(\mathbf{r})$ are the electron densities of the pure graphene (or vacancy graphene) and the isolated Mo, calculated separately with the same atomic positions and supercell size as in the corresponding Mo/graphene systems. From the charge redistribution, CDD analysis can provide insights into the strength and nature (i.e., ionic or covalent) of the interaction between Mo and its surroundings.

In in-plane doping cases (MoG and d1Mo, Figure 6a,d), electron transfer occurs from Mo to carbon atoms, accumulating in the σ orbitals of nearby carbons, suggesting that the Mo—C interaction forms ionic bonds.

For Mo(T) and Mo(H) (Figure 6b,c), the donated charge accumulates mainly in the π orbitals of the carbon atoms beneath the adatom, with some delocalization across the graphene matrix. The bonding charge between Mo's *d*-orbitals and the surrounding C_{pz} atoms indicates covalent bond formation.

The adsorption of Mo on a single vacancy (Mod1) leads to the ionic bond formation, while on N/S-decorated monovacancies (Mo*d1N3/Mo*d1S3), strong covalent bonds form, as shown by the bonding charge accumulation (Figure 6e–g). In Mod1, charge accumulates primarily in the σ orbitals of the three coordinating carbon atoms, whereas in Mo*d1N3 and Mo*d1S3, charge density increases on nitrogen, sulfur, and their directly linked carbon atoms.

3.6.2. Band Structure Analysis

The effects of charge redistribution and hybridization are reflected in the *k*-resolved electronic bands shown in Figure 8 and 9. Typically, electronic bands characterized by *s* and *p* orbitals have a parabolic shape. In graphene, these bands are linear at the Fermi level. Transition metals like molybdenum, with localized *d* bands, display flat bands. However, in Mo-modified graphene, *p*–*d* hybridization causes linear and parabolic bands to shift into quasiflat bands, especially near *d*-character bands.

Based on the hybridization between the *d* shells of a transition metal (TM) and the defect levels associated with the unreconstructed D_{3h} carbon vacancy, Santos et al.[41] proposed a hybridization model (HBD model) to describe the band structure of metal adsorption on monovacancy graphene. According to the model, the *d* states of the metal atom interact with the localized dangling bond defect states of the unreconstructed D_{3h} monovacancy graphene to form hybrid defect states near the Fermi level. The interested reader can see ref. [41].

The calculated band structure for the D_{3h} monovacancy is depicted in **Figure 7**, showing the sp and pz orbital defect levels. The HBD scheme is evident for both Mo*d1 (Mo adsorbed on a single vacancy, **Figure 8**) and MoG (Mo substitutional doping, Figure 8) electrode structures. Consistent with the model, three localized defect levels are observed in both MoG (Figure 8a) and Mo*d1 (Figure 8b). Specifically, in MoG, two of these are the bonding–antibonding σ–*d* pairs (represented by the weighted blue bands), while the third is a nonbonding defect state.

For the MoG electrode (substitutional doping), the enhancement of C_Q at the cathode is primarily attributed to the nonbonding defect state (gray bands at E_f), which arises from significant contributions by the Mo *s* and dz^2 orbitals. Additionally, states

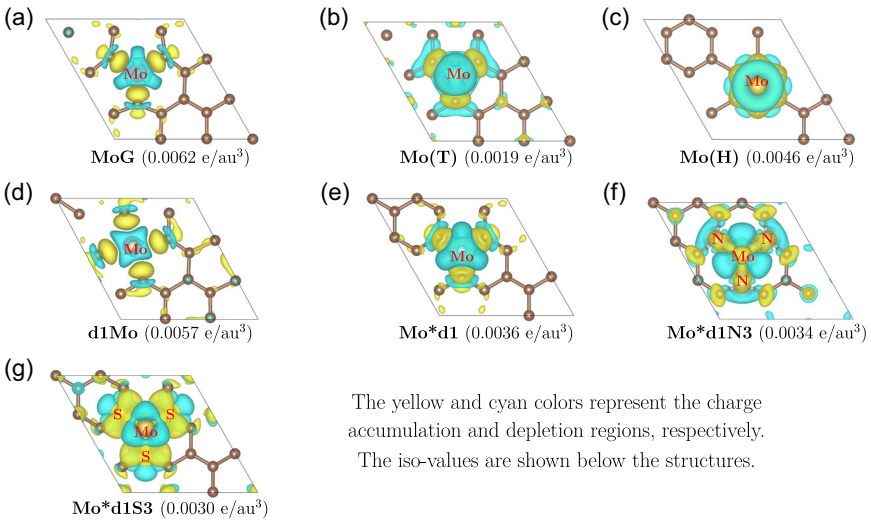

Figure 6. Density difference maps ($\Delta\rho$) illustrating the charge redistribution for various Mo-graphene systems. a) Mo substituting a carbon atom in pristine: *MoG*. b) Mo adsorbed on top site: *Mo(T)*. c) Mo adsorbed on hollow site: *Mo(H)*. d) Mo substituting one unbonded C atom in single vacancy defect: *d1Mo*. e) Mo adsorbed on single vacancy defect: *Mo*d1*. f) Mo adsorbed on d1N3, where 3 unbonded C atoms in d1 are replaced with nitrogen: *Mo*d1N3*. g) Mo adsorbed on d1S3, where 3 unbonded C atoms in d1 are replaced with sulfur: *Mo*d1S3*.

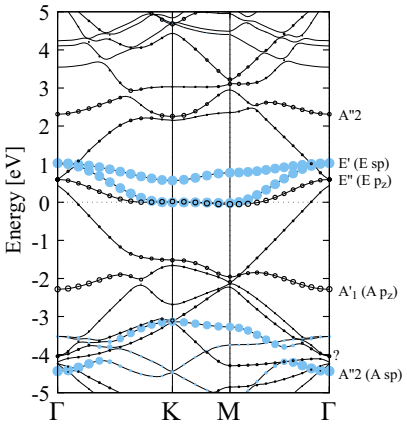

Figure 7. Calculated nonpolarized band structure of an unoptimized D_{3h} monovacancy in a $3 \times 3 \times 1$ supercell of graphene. Weighted blue bands have *sp* contributions, and open circle bands have *pz* character.

resulting from the hybridization between the C*pz* orbitals of the coordinating carbon atoms and the Mo d*zx* and d*zy* orbitals (salmon bands) also play a role in the capacitance enhancement. In contrast, the bonding–antibonding *σ*–*d* states (represented by the blue bands) are located far from the Fermi level and thus do not contribute to C_Q enhancement within the energy range relevant for aqueous electrolytes.

Decomposing the nonbonding defect band (from K to Γ) in MoG (within ±1.00 eV) reveals the wavefunctions contributing to the charge density, confirming that the Mo *s* and Mo dz^2 orbitals are indeed not bonded to any atom (Figure 8a). Furthermore, this decomposition shows that the C_π states of the carbon atoms directly linked to those neighboring Mo contribute to the improved C_Q. The DOS and the spatial distribution of the nonbonding defect state indicate that electrons mainly trapped in the hybridized Mo *s* and dz^2 states will be extracted when the electrode is positively charged.

Quantum capacitance improvement in the energy range of interest (±1.00 eV) for Mo*d1 (Mo adsorbed on single vacancy) is primarily attributed to the *p*–*d* spin-up and spin-down nonbonding defect levels (blue bands), consisting mainly of Mo *d* states, except for dz^2. This is confirmed by the band decomposed isosurface plot in the insert. Additionally, C_Q improvement at the conduction band is influenced by antibonding defect states with Cσ–4dz^2 and 4*s* character (red band at ≈0.80 eV). Excess electrons would be injected into spin-up and spin-down bonding defect states (salmon band around 1.0 eV), as visualized in the isosurface plot.

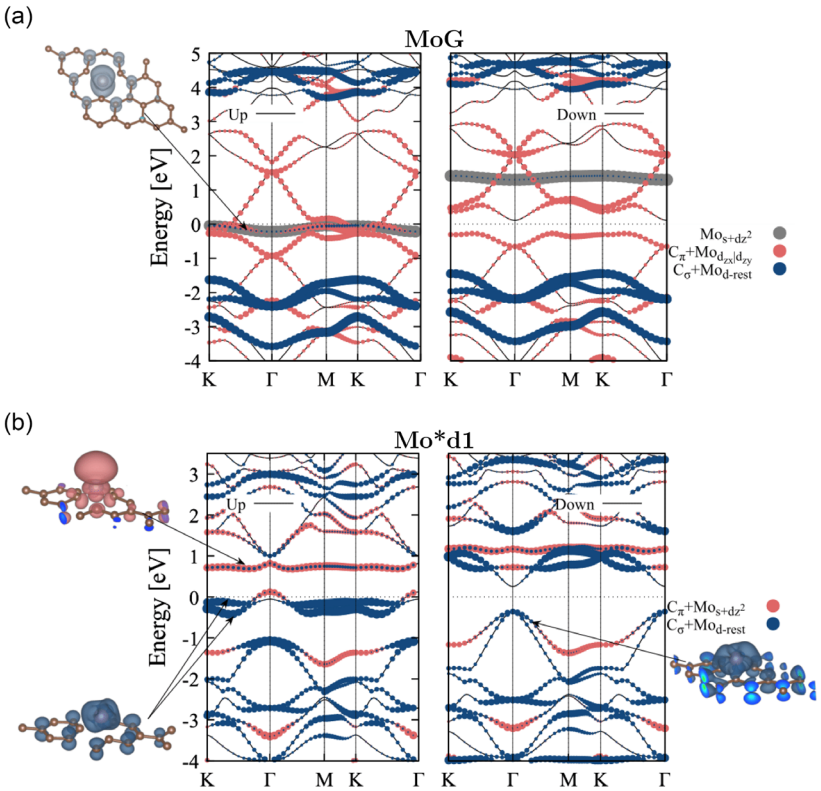

Figure 8. k-resolved band structure of a) MoG: Gray dots represent contributions from the 4dz^2 and *s* orbitals of the Mo atom. Soft red dots represent a combination of the C2*pz* orbitals from neighboring C atoms and the 4d*xz* and 4d*yz* Mo orbitals. Blue dots represent contributions from the remaining 4dx^2–y^2 and 4d*xy* orbitals, along with the C2*px* and C2*py* orbitals. b) Mo*d1: Soft red dots represent contributions from the 4s and 4dz^2 orbitals of Mo and the Cp$_z$ states of neighboring C atoms, while blue dots represent contributions from the remaining four *d* states of Mo and the Cp$_x$ and Cp$_y$ states of neighboring C atoms. The inset shows a visualization of the contributions of selected wavefunctions on specific bands to the charge density. The size of the colored dots indicates the relative magnitude of each contribution. The Fermi level is set to 0 eV.

The Fermi level lies in the bandgap for MoG and Mo*d1 in the spin-down band structure, while their spin-up bands exhibit metallic behavior, indicating that both are half-metals. The HBD scheme by Santos et al.[41] does not apply to the rest of the band structures because they do not have the required symmetry and due to differences in their chemical environments. A different k-path is chosen for d1Mo (Mo doped at a d1 vacancy site) as its band structure did not fully agree with the DOS plot (**Figure 9**a). Unlike MoG and Mo*d1, the dz^2 of Mo in d1Mo hybridized with other d orbitals, forming a strongly localized d band (salmon color band), inducing spin polarization.

Between ±1.00 eV, the localized d band (salmon-weighted bands) of the spin-up band structure contributes most to the C_Q enhancement, alongside the delocalized π electrons in graphene's parabolic bands. In this energy range, electrons in the σ orbitals of carbon atoms directly attached to Mo (where charge accumulation occurs) play a minimal role in improving C_Q. The Fermi level crossing the energy bands confirms the metallic behavior.

For Mo adsorption at both the top (Mo(T)) and hollow (Mo(H)) sites of graphene, the σ orbitals, responsible for graphene's structural stability, do not contribute to its electronic properties, as expected. The linear C_π bands hybridize with d bands, turning

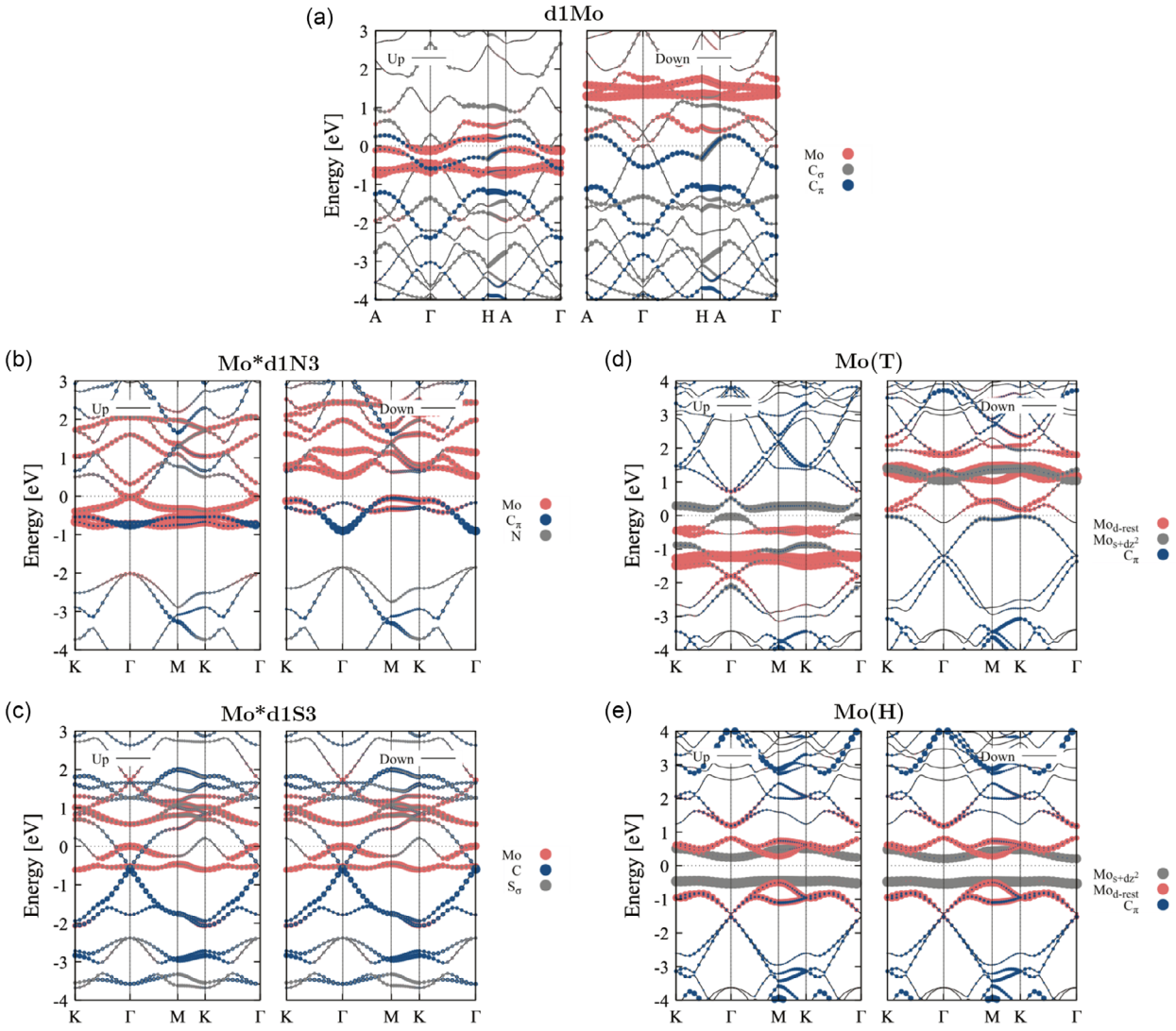

Figure 9. k-resolved band structure of a) d1Mo: Colored dots represent the contributions from Mo states (soft red), the σ states of neighboring carbon atoms (gray), and the π states of neighboring carbon atoms (gray). The points A and H are located at the edges of the Brillouin zone, with A at the top along the c-axis and H on the hexagonal face. b) Mo*d1N3: Colored dots represent contributions from Mo states (soft red), states of neighboring N atoms (gray), and the π states of C atoms directly bonded to N (blue). c) Mo*d1S3: Colored dots represent contributions from Mo states (soft red), σ states of neighboring S atoms (gray), and states of C atoms directly bonded to S (blue). d) Mo(T): Colored dots represent the contributions from Mo states (soft red and gray) and the π states of the C atoms directly beneath the adatom (blue). e) Mo(H): Colored dots represent contributions from Mo states (soft red and gray) and the π states of the carbon atoms directly beneath the adatom (blue). The size of the colored dots represents the relative magnitude of the contribution. Fermi level set to 0 eV.

the linear dispersion near the Fermi level into semiflat bands and introducing defect states. Localized Mo states in Mo(T) induce spin polarization, whereas Mo at the hollow site (Mo(H)) is nonmagnetic, exhibiting semiconducting behavior. Mo(T), on the other hand, shows metallic behavior. The *pz* states of the carbon atoms directly below the adatom are sparsely distributed within the energy range of concern (±1.00 eV)—particularly in Mo(T)—and are largely situated outside this range. This indicates that the electrons transferred to and shared with the carbon atoms do not significantly contribute to capacitance enhancement. Instead, defect bands with dz^2 and *s* character (gray-weighted bands), along with the remaining *d* orbitals (salmon color bands), make the most significant contribution to C_Q improvement. The degree of π–*d* orbital overlap suggests that Mo(H) forms a stronger bond than Mo(T).

k-resolved bands for Mo*d1S3 and Mo*d1N3, shown in Figure 9b,c, reveal contributions from Mo, N/S, and the carbon atoms linked to these heteroatoms. Mo*d1S3 is nonmagnetic, while localized states of Mo in Mo*d1N3 induce spin polarization, though both structures exhibit metallic behavior. After charge redistribution in Mo*d1N3, the Cπ orbitals (showing charge accumulation), along with the localized Mo *d* orbitals, significantly enhance C_Q. Nitrogen contributes less to this improvement.

For Mod1S3, S_π states do not enhance capacitance (within ±1.00 eV). Instead, localized Mo states and contributions from carbon atoms bonded to sulfur drive C_Q enhancement. Both Mo*d1N3 and Mo*d1S3 show notable *p*–*d* hybridization, as indicated by the charge redistribution in the CDD plots, semiflat bands in the band structure, and substantial orbital overlap.

Recent studies have shown that transition metal species can undergo proton-coupled electron transfer (PCET), where the metal center typically accepts an electron and the ligand donates a proton (H^+).[42] As illustrated in Figure 6a, the electron-deficient (positively charged) Mo centers in the CDD plots may facilitate electron acceptance, while the electron-rich ligand regions (notably in Mo*d1S3 and Mo*d1N3) could donate electrons to vacant H^+ orbitals in aqueous electrolytes. Djire group[43] demonstrated that nanostructured γ-Mo_2N in aqueous H_2SO_4 exhibited pseudocapacitance due to PCET and Mo redox reactions. Thus, the Mo-modified electrodes in this study may similarly possess pseudocapacitive properties.

3.7. Structural Stability Investigation

The formation energies (E_{form}) of the various structures, including graphitic-X doping, single vacancy, three X atoms with monovacancy, and X doping at the monovacancy site are calculated and visually represented in **Figure 10**a (X = N/S/Mo). The energies, E_{form}, are obtained using the formulas

$$E_{XG} = E_{defect\text{-}Gra} - (n-1)\mu_C - \mu_X \quad (5)$$

$$\Delta E_{d1X3} = E_{defect\text{-}Gra} - (n-3)\mu_C - 3\mu_X \quad (6)$$

$$\Delta E_{d1X} = E_{defect\text{-}Gra} - (n-1)\mu_C - \mu_X \quad (7)$$

$$\Delta E_{d1} = E_{defect\text{-}Gra} - n\mu_C \quad (8)$$

where ΔE_{XG}, ΔE_{d1X3}, ΔE_{d1X}, and ΔE_{d1} are the formation energies of graphitic-X doping, three X atoms at monovacancy sites, single X doping at monovacancy site, and single vacancy, respectively. $E_{defect\text{-}Gra}$ is the total energy of the doped or monovacancy defect graphene with *n* number of atoms. For X = N, μ_N is the total energy per atom of N_2 molecule, and $\mu_{S/Mo}$ (X = S/Mo) is the energy per S/Mo atom in a bulk sulfur/molybdenum crystal. μ_C is the total energy per atom of pristine graphene.

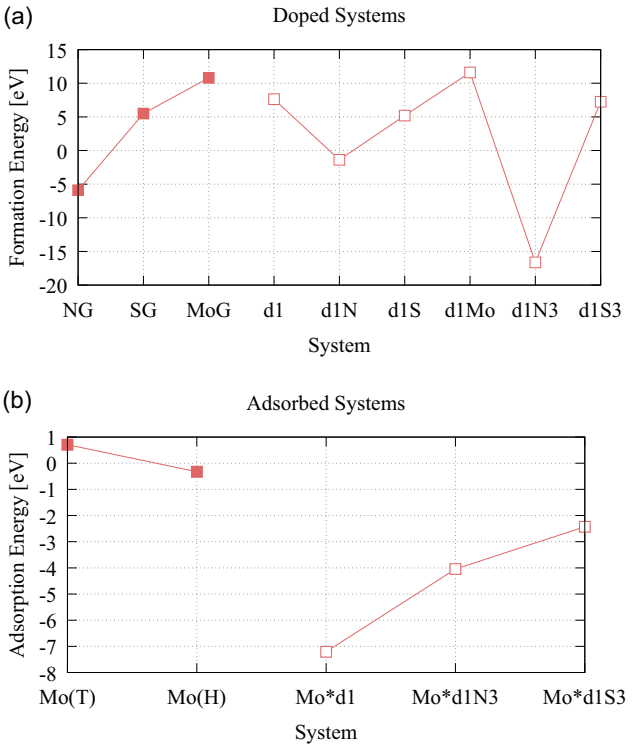

Figure 10. a) Formation energies (E_{form}) and b) adsorption energies (E_{ad}) of various Mo-modified systems.

From the trend observed in Figure 10a, the stability for the graphitic doping reduces with increasing dopant atomic size; hence, substitutional doping of Mo in graphene (MoG) is the least stable (10.8 eV) and nitrogen-doped graphene (NG) is the most stable (−5.9 eV). SG has a formation energy of 5.49 eV, in agreement with the report of Hajibaba and coworkers.[44]

When a carbon atom is removed from graphene and the structure relaxed, one of two outcomes is possible: either the broken bonds remain unsaturated or the monovacancy undergoes Jahn-Teller rearrangement and two dangling bond carbon atoms reorient to form a covalent bond, leaving a single unbonded C atom. The former occurred for the d1 structure reported here, with the symmetry modified from the unreconstructed D_{3h} to a C_{2v} symmetry and a formation energy of 7.6 eV, as shown in Figure 10a. This is in agreement with other PBE theoretical results.[45,46] Monovacancies are not stable and easily move within the graphene plane and stabilize when they encounter another monovacancy, leading to the formation of a divacancy defect.[46,47] If we use this as a benchmark to relate to the degree of instability, revealed by the formation energies of the vacancy-doped materials (open box in Figure 10a), it suggests that d1N3, d1N, d1S, and d1S3 (in decreasing order of stability) will be more likely to form and more stable than single vacancy defect. d1Mo

(11.6 eV) is the most unstable, likely due to stress introduced by the large size of Mo.

The adsorption energies (E_{ads}) for Mo anchored on the various substrates are shown in Figure 10b. The energies were obtained using the formula

$$E_{ad}(\mathrm{Mo}) = E_{subs+Mo} - E_{subs} - E_{Mo} \quad (9)$$

$E_{subs+Mo}$, E_{subs}, and E_{Mo} are the total energy of the optimized Mo-on-substrate system, total energy of the substrate without the Mo adatom, and total energy of an isolated Mo atom, respectively. Mo(T) adsorption energy is 0.71 eV (Figure 10b), whereas Mo(H) has a relatively strong adsorption energy of −0.32 eV. The interaction between graphene and Mo is stronger in Mo(H) than Mo(T) and consequently more stable. For the trend observed in Mo anchored on vacancy substrate, molybdenum over single vacancy (Mo*d1) has a stronger interaction and more stable, with a formation energy of −7.20 eV, in agreement with the typical energy value (≈−7 eV) for transition metal loaded on graphene.[48,49] This is followed by Mo*d1N3 (−4.04 eV) and finally, Mo*d1S3 (−2.43 eV). Nonetheless, Mo over vacancy defect will be more stable than adsorbed over pristine graphene.

4. Conclusions

In summary, the effects of Mo, S, N, and single-vacancy modification on structural, electronic, and energy storage properties (C_Q and Q_{SCD}) of graphene were explored using DFT calculations. Fifteen graphene electrode models were studied, involving graphitic doping, monovacancy doping, and adsorption of Mo on pristine and single vacancy structures. The results show that doping can improve C_Q of graphene. Although single vacancy (d1) modification enhances C_Q, models with single and triple pyridinic nitrogen (d1N and d1N3) exhibited even higher C_Q. Additionally, pyrrolic sulfur (d1S) significantly limits C_Q of graphene but triple pyridine-S exhibits better performance. The presence of sulfur also tended to quench the magnetic moment of Mo and the C vacancy.

Overall, electrodes involving Mo exhibit the greatest C_Q, with Mo adsorbed on the top site yielding the highest C_Q. However, the formation and adsorption energy calculation indicate that Mo adsorption on the hollow site was more likely than on the top site. Ultimately, to utilize Mo, the best approach would be to load Mo on vacancy/N or S decorated vacancy site. The $4dz^2$ and 4s states of Mo play major roles in improving C_Q, and positive and negative charge accumulation around Mo may facilitate proton-coupled electron transfer.

It is important to recognize the potential trade-offs between improved quantum capacitance and the risk of electrolyte instability. While a higher C_Q is advantageous for energy storage, the increased reactivity of the electrode material, particularly in systems containing certain defects or dopants, may lead to unwanted catalytic effects. For instance, the presence of unbonded atoms, as in some vacancy-modified or pyridinic nitrogen-doped structures, can introduce highly reactive σ states, which may promote undesirable electrolyte decomposition during cycling.[23] This is especially relevant for high-performance applications like lithium-ion capacitors (LICs) where stability is critical. These findings provide strategies for designing stable graphene-based supercapacitor electrode materials with high C_Q and pseudocapacitance-active sites for energy storage.

Acknowledgements

The computations and data handling were enabled by resources provided by the South African Center for High Performance Computing (CHPC) and one of the authors, David, is grateful. The authors also acknowledge the Government of Ghana Book and Research Allowance (BRA) support.

Conflict of Interest

The authors declare no conflict of interest.

Author Contributions

Henry Martin: Conceptualization; Investigation; Methodology; Formal analysis; Software visualization. **Linus K. Labik**: Formal Analysis; Editing; Validation.

Data Availability Statement

The data that support the findings of this study are available from the corresponding author upon reasonable request.

Keywords

defects in solids, doping, graphenes, molybdenums, quantum capacitance, supercapacitors

Received: September 3, 2024
Revised: October 22, 2024
Published online:

[1] P. Simon, Y. GoGotSi, *Nat. Mater.* **2008**, *7*, 845.
[2] C. G. Liu, Z. N. Yu, D. Neff, A. Zhamu, B. Z. Jang, *Nano Lett.* **2010**, *10*, 4863.
[3] X. W. Yang, C. Cheng, Y. F. Wang, L. Qiu, D. Li, *Science* **2013**, *341*, 534.
[4] J. J. Yoo, K. Balakrishnan, J. S. Huang, V. Meunier, B. G. Sumpter, A. Srivastava, M. Conway, A. L. M. Reddy, J. Yu, R. Vajtai, *Nano Lett.* **2011**, *11*, 1423.
[5] B. G. Choi, J. Hong, W. H. Hong, P. T. Hammond, H. Park, *ACS Nano* **2011**, *5*, 7205.
[6] X. Yu, S. Yun, J. S. Yeon, P. Bhattacharya, L. Wang, S. W. Lee, X. Hu, H. S. Park, *Adv. Energy Mater.* **2018**, *8*, 1702930.
[7] K. S. Novoselov, A. K. Geim, S. V. Morozov, D. Jiang, Y. Zhang, S. V. Dubonos, I. V. Grigorieva, A. A. Firsov, *Science* **2004**, *306*, 666.
[8] K. S. Novoselov, A. K. Geim, S. V. Morozov, D. Jiang, M. I. Katsnelson, I. V. Grigorieva, S. V. Dubonos, A. A. Firsov, *Nature* **2005**, *438*, 197.
[9] X. Li, W. Cai, J. An, S. Kim, J. Nah, D. Yang, R. Piner, A. Velamakanni, I. Jung, E. Tutuc, *Science* **2009**, *324*, 1312.
[10] Y. Zhu, S. Murali, M. D. Stoller, K. J. Ganesh, W. Cai, P. J. Ferreira, A. Pirkle, R. M. Wallace, K. A. Cychosz, M. Thommes, *Science* **2011**, *332*, 1537.
[11] X. Fan, W. T. Zheng, J.-L. Kuo, *ACS Appl. Mater. Interfaces* **2012**, *4*, 2432.
[12] E. Yoo, J. Kim, E. Hosono, *Nano Lett.* **2008**, *8*, 2277.

[13] Y. Wang, Z. Shi, Y. Huang, Y. Ma, C. Wang, M. Chen, Y. Chen, *J. Phys. Chem. C* **2009**, *113*, 13103.
[14] S. Ghosh, S. K. Behera, A. Mishra, C. S. Casari, K. K. Ostrikov, *Energy Fuels* **2023**, *37* 17836.
[15] S. Luryi, *Appl. Phys. Lett.* **1988**, *52*, 501.
[16] E. Paek, A. J. Pak, G. S. Hwang, *J. Electrochem. Soc.* **2013**, *160*, A1.
[17] E. Paek, A. J. Pak, K. E. Kweon, G. S. Hwang, *J. Phys. Chem. C* **2013**, *117*, 5610.
[18] J. Xia, F. Chen, J. Li, *Nat. Nanotechnol* **2009**, *4*, 505.
[19] M. D. Stoller, C. W. Magnuson, Y. W. Zhu, S. Murali, J. W. Suk, R. Piner, R. S. Ruoff, *Energy Environ. Sci.* **2011**, *4*, 4685.
[20] G. M. Yang, H. Z. Zhang, X. F. Fan, W. T. Zheng, *J. Phys. Chem. C* **2015**, *119*, 6464.
[21] G. Lota, K. Lota, E. Frackowiak, *Electrochem. Commun.* **2007**, *9*, 1828.
[22] T. P. Smith, B. B. Goldberg, P. J. Stiles, M. Heiblum, *Phys. Rev. B* **1985**, *32*, 2696.
[23] F. Su, L. Huo, Q. Kong, L. Xie, C. Chen, *Catalysts* **2018**, *8*, 10.
[24] C. Özdoğan, H. Kökten, *FlatChem* **2022**, *31*, 100313.
[25] S. Ghosh, S. Barg, S. M. Jeong, K. Ostrikov, *Adv. Energy Mater.* **2020**, *10*, 17836.
[26] L. Wen, C. Ren, Y. Zou, W. Lin, K. Ding, *Appl. Surf. Sci.* **2020**, *534*, 147595.
[27] Y. Qin, S. Zhang, G. Gao, S. Ding, Y. Su, *Mol. Catal.* **2022**, *517*, 112048.
[28] J. Li, B. Zhang, Q. Song, X. Xu, W. Hou, *Ceram. Int.* **2020**, *46*, 14178.
[29] C. Zhan, C. Lian, Y. Zhang, M. W. Thompson, Y. Xie, J. Wu, P. R. C. Kent, P. T. Cummings, D. Jiang, D. J. Wesolowski, *Adv. Sci.* **2017**, *4*, 1700059.
[30] P. Hohenberg, W. Kohn, *Phys. Rev.* **1964**, *136*, B864.
[31] W. Kohn, L. J. Sham, *Phys. Rev.* **1965**, *140*, A1133.
[32] M. D. Radin, T. Ogitsu, J. Biener, M. Otani, B. C. Wood, *Phys. Rev. B* **2015**, *91*, 03.
[33] P. Giannozzi, S. Baroni, N. Bonini, M. Calandra, R. Car, C. Cavazzoni, D. Ceresoli, G. L. Chiarotti, M. Cococcioni, I. Dabo, A. Dal Corso, S. de Gironcoli, S. Fabris, G. Fratesi, R. Gebauer, U. Gerstmann, C. Gougoussis, A. Kokalj, M. Lazzeri, L. Martin-Samos, N. Marzari, F. Mauri, R. Mazzarello, S. Paolini, A. Pasquarello, L. Paulatto, C. Sbraccia, S. Scandolo, G. Sclauzero, A. P. Seitsonen, et al., *J. Phys.: Condens.Matter* **2009**, *21*, 395502 (19pp).
[34] P. E. Blöchl, *Phys. Rev. B* **1994**, *50*, 17953.
[35] G. Kresse, D. Joubert, *Phys. Rev. B* **1999**, *59*, 1758.
[36] D. D. Johnson, *Phys. Rev. B* **1988**, *38*, 12807.
[37] J. D. Head, M. C. Zerner, *Chem. Phys. Lett.* **1985**, *122*, 264.
[38] N. Marzari, D. Vanderbilt, A. De Vita, M. C. Payne, *Phys. Rev. Lett.* **1999**, *82*, 3296.
[39] J. Zhu, H. Park, R. Podila, A. Wadehra, P. Ayala, L. Oliveira, J. He, A. A. Zakhidov, A. Howard, J. Wilkins, A. M. Rao, *J. Magn. Magn. Mater.* **2016**, *401*, 70.
[40] P. Dianat, in *Photodetectors* (Ed: B. Nabet), Woodhead Publishing, Sawston, Cambridge, UK **2016**, pp. 471–510.
[41] E. J. G. Santos, A. Ayuela, D. Sánchez-Portal, *New J. Phys.* **2010**, *12*, 053012.
[42] J. M. Mayer, *Acc. Chem. Res.* **2011**, *44*, 36.
[43] A. Djire, J. B. Siegel, O. Ajenifujah, L. He, L. T. Thompson, *Nano Energy* **2018**, *51*, 122.
[44] S. Hajibaba, S. Gholipour, M. Pourjafarabadi, A. Bakhshayesh, M. M. Byranvand, M. Saliba, Y. Abdi, *J. Energy Storage* **2024**, *79*, 110044.
[45] A. M. Valencia, M. J. Caldas, *Phys. Rev. B* **2017**, *96*, 125431.
[46] F. Banhart, J. Kotakoski, A. Krasheninnikov, *ACS Nano* **2011**, *5*, 26.
[47] L. E. F. Foa Torres, S. Roche, J. Charlier, in *Introduction To Graphene-Based Nanomaterials: From Electronic Structure To Quantum Transport*, Cambridge University Press, Cambridge, England **2014**.
[48] J. Kang, H. Deng, S. Li, J. Li, *J. Phys.: Condens.Matter* **2011**, *23*, 346001.
[49] A. V. Krasheninnikov, P. O. Lehtinen, A. S. Foster, P. Pyykkö, R. M. Nieminen, *Phys. Rev. Lett.* **2009**, *102*, 126807.